Design of A Lightweight Robotic Tensegrity Morphing Airfoil

Luyang Zhao*
Department of Electrical and Computer Engineering, Clemson University, Clemson, SC, 29634

Yitao Jiang, Chun-Yi She, Devin Balkcom†
Department of Computer Science, Dartmouth College, NH, 03755

Haibo Dong‡
Department of Mechanical and Aerospace Engineering, University of Virginia, VA, 22904

Muhao Chen§
Department of Mechanical and Aerospace Engineering, University of Houston, Houston, TX, 77204

This paper explores the design and fabrication of a robotic airfoil based on a tensegrity morphing structure. We begin by introducing a family of tensegrity morphing airfoil designs that convert a continuous airfoil shape into a discrete configuration. The airfoil structure is divided into two main components: a rigid section (the D-section head) and a flexible section (the tensegrity morphing tail). We compute aerodynamic forces using the panel method and, based on the drag and lift analyses, propose a morphing airfoil design and develop its CAD model. This model integrates all essential electronics, including the battery, PCB board, and motors, within the rigid D-section. The flexible tail is actuated by strings, enabling adaptive morphing. Our approach integrates lightweight tensegrity principles with adaptive design to create efficient morphing airfoil structures. The methodology is also applicable to bio-inspired wings, robotic fingers, grippers, and other soft robotic systems.

Nomenclature

n_n	=	Total number of nodes in a tensegrity structure
$\boldsymbol{n} \in \mathbb{R}^{3n_n}$	=	Nodal coordinate vector for all the nodes
n_a	=	Number of free nodes in the structure
$\boldsymbol{n}_a \in \mathbb{R}^{3n_a}$	=	Nodal coordinate vector for free nodes
$\boldsymbol{E}_a \in \mathbb{R}^{3n_n \times 3n_a}$	=	Index matrix extracting $\boldsymbol{n}_a$ from $\boldsymbol{n}$; $\boldsymbol{n}_a = \boldsymbol{E}_a^\top \boldsymbol{n}$
n_e	=	Number of structural elements (bars and strings)
$\boldsymbol{C} \in \mathbb{R}^{n_e \times n_n}$	=	Connectivity matrix for the structural elements
$\boldsymbol{M} \in \mathbb{R}^{3n_n \times 3n_n}$	=	Mass matrix in the nonlinear dynamics
$\boldsymbol{K} \in \mathbb{R}^{3n_n \times 3n_n}$	=	Stiffness matrix in the nonlinear dynamics
$\boldsymbol{g} \in \mathbb{R}^{3n_n}$	=	Gravity vector in the nonlinear dynamics
$\boldsymbol{D} \in \mathbb{R}^{3n_n \times 3n_n}$	=	Damping matrix in the nonlinear dynamics
$\boldsymbol{f}_{\text{ex}} \in \mathbb{R}^{3n_n}$	=	External force vector in the nonlinear dynamics
$\boldsymbol{m} \in \mathbb{R}^{n_e}$	=	Mass vector for all the structural elements
$\boldsymbol{l} \in \mathbb{R}^{n_e}$	=	Length vector for all the structural elements
$\boldsymbol{l}_0 \in \mathbb{R}^{n_e}$	=	Rest length vector for all the structural elements
$\hat{\boldsymbol{v}}$	=	Converts vector $\boldsymbol{v}$ to a diagonal matrix
$\boldsymbol{x} \in \mathbb{R}^{n_e}$	=	Force density (force per unit length) vector for all the structural elements
g	=	Gravitational constant, $9.80\,\text{m/s}^2$
$\lvert\boldsymbol{V}\rvert$	=	Absolute values of each element in matrix $\boldsymbol{V}$

*Assistant Professor, Department of Electrical and Computer Engineering, Clemson University, and AIAA Member.
†Graduate Students, and Professor, Department of Computer Science, Dartmouth College, and AIAA Member.
‡Professor, Department of Mechanical and Aerospace Engineering, University of Virginia, and AIAA Member.
§Assistant Professor, Department of Mechanical and Aerospace Engineering, University of Houston, and AIAA Member.

$\boldsymbol{E}_t \in \mathbb{R}^{n_e}$ = Tangent modulus vector for all the structural elements
$\boldsymbol{A} \in \mathbb{R}^{n_e}$ = Cross-sectional area for all the structural elements
$b.d.(\boldsymbol{V})$ = Converts matrix $\boldsymbol{V}$ into a block diagonal matrix

I. Introduction

A tensegrity structure consists of a network of compressive components (bars or struts) and tensile elements (strings or cables) [1–3]. A major characteristic of tensegrity structures is the axial loading of one-dimensional elements, which supports the strategic placement of materials along the main load paths, thereby minimizing the overall mass of the system [4–6]. This loading introduces uncertainty only in the axial direction, improving modeling accuracy and control compared with bending, which creates uncertainty in multiple directions [3]. The prevalence of tensile elements in these structures enhances their capabilities for shape adaptation [7]. Accurate modeling and shape-morphing capabilities are essential for morphing airfoils [8]. Recent developments have expanded the use of tensegrity principles across various fields, including materials, flexible structures, and robotics, leading to innovations in metamaterials [9], sensors [10, 11], spinal models [12], rovers [13], towers [14], robotic manipulators [15, 16], swimming robots [17–19], climbing robots [20], self-assembling modular robots [21–23], toroidal structures [24, 25], space antennas [14], and planetary landers [26].

Morphing airfoils are increasingly garnering interest over traditional rigid airfoils due to their adaptability across various flight conditions, promising notable advantages in flexibility and efficiency. Traditional methods such as flaps, slats, ailerons, and winglets, while effective in achieving specific control objectives [27, 28], often disrupt the optimally designed aerodynamic profile of airfoils. In contrast, emerging technologies like shape memory alloys and piezoelectric actuators offer smoother transitions but tend to operate at lower bandwidths and require substantial support equipment [29, 30]. An integrated approach, combining structural and control design, is also emerging. For instance, Chen et al. introduced a design incorporating tensegrity for morphing airfoils alongside a nonlinear control strategy for class-k tensegrity structures [31]. Similarly, Shintake et al. developed a bio-inspired tensegrity system for a robotic fish powered by waterproof servomotors [32]. Mills et al. evaluate tensegrity aircraft wing designs against conventional wings, demonstrating that optimized tensegrity systems achieve comparable structural performance at reduced weight, highlighting their potential for morphing aerospace structures [33]. Zhou et al. showed an active tensegrity morphing wing with distributed pneumatic actuators that enables precise shape control and improved aerodynamic performance, validated through simulations and wind tunnel experiments [34]. Liu et al. introduced a tensegrity camber morphing airfoil that enables smooth camber changes [35]. However, few studies address the structural and control challenges integratively from a systems perspective. This research explores the feasibility of designing and fabricating a lightweight tensegrity-based robotic airfoil capable of smooth, precise bending.

The paper is organized as follows: Section II covers the design and aerodynamic performance of tensegrity morphing airfoils. Section III outlines experimental design and testing. Section IV summarizes the findings.

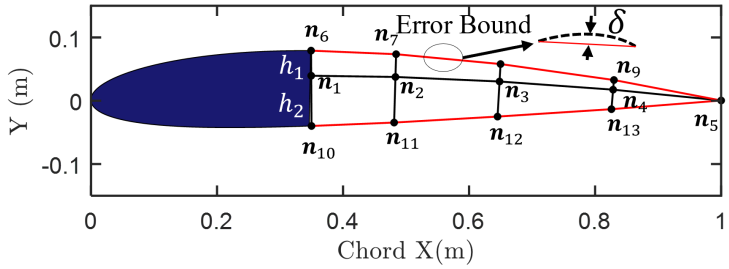

Fig. 1 Notations of the tensegrity airfoil (NACA 2412). Tensegrity airfoil configuration: the blue area is the D-Section, and the black and red lines are bars and strings. The error bound δ is 0.001 m. The structure complexity q is 4.

II. Design of Tensegrity Morphing Airfoils

The tensegrity airfoil is divided into two parts: a rigid head (commonly referred to as the D-Section) and a flexible tail (the tensegrity structure). The rigid head houses the electronics and maintains a continuous profile to ensure a

smooth airfoil shape. In contrast, the flexible tail, designed for shape adaptation, is a discrete structure. The discrete nodes of the flexible tail align with the airfoil's continuous profile. The tensegrity structure provides support for these nodes, enabling controlled shape changes. Tensegrity morphing airfoils apply tensegrity principles for dynamic shape adaptation via strings. Inspired by fish vertebrae, our design is presented as follows.

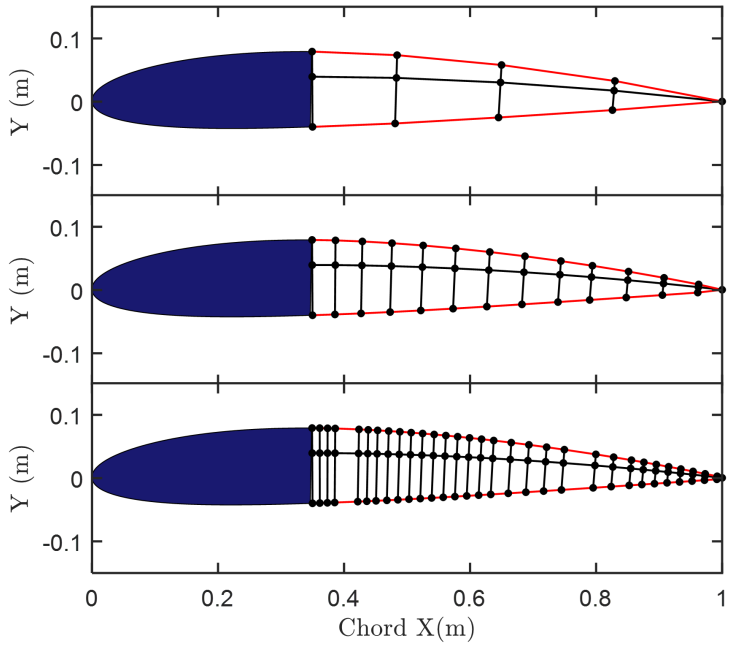

Fig. 2 Tensegrity airfoil configurations with varying error bounds from top to bottom $\delta = 1 \times 10^{-3}$ m, 1×10^{-4} m, and 1×10^{-5} m.

The nodal matrix is defined as $\boldsymbol{N} = [\boldsymbol{n}_1, \boldsymbol{n}_2, \cdots, \boldsymbol{n}_{3q+1}]$, where q represents the structural complexity, corresponding to the number of horizontal line segments. The matrices $C_{b_{in}}$ and $C_{s_{in}}$ each contain rows with two elements, specifying the start and end nodes of each bar or string. The connectivity of the bars and strings can be expressed using the node indices as follows:

$$C_{b_{in}} = \begin{cases} [i, i+1], \ 1 \le i \le q \\ [i-q, i+1], \ q+1 \le i \le 2q \\ [i-2q, i+1], \ 2q+1 \le i \le 3q \end{cases}, \ C_{s_{in}} = \begin{cases} [i+1+q, i+2+q], \ 1 \le i \le q-1 \\ [i+1+2q, i+2+2q], \ 1 \le i \le q-1 \\ [2q+1, q+1], \ [3q+1, q+1] \end{cases}. \tag{1}$$

We use the error-bound method [31] to generate discrete points on the airfoil, ensuring that the maximum deviation between the continuous and discrete airfoil profiles does not exceed a specified value δ, referred to as the error bound, as shown in Fig. 1. By varying δ, we achieve different morphing airfoil configurations, as depicted in Fig. 2.

The error-bound method applies to any tensegrity morphing airfoil. In this study, we use a NACA 2412 airfoil profile as an example, with a chord length of 1 m. The airfoil features a rigid D-section extending from 0 to 0.35 m, followed by a flexible tensegrity tail. The design includes two bars, where h_1 and h_2 represent their vertical distances from the upper and lower curves, respectively. In the tensegrity section, the ratio of these vertical distances ($h_1 = |\boldsymbol{n}_{6,y} - \boldsymbol{n}_{1,y}|$ and $h_2 = |\boldsymbol{n}_{1,y} - \boldsymbol{n}_{10,y}|$) is set to $h_2/h_1 = 2$, inducing a downward bending tendency. Note that this design follows the camber-line concept, and the value can be adjusted to meet the required bending stiffness and deformation performance.

To analyze the influence of a discrete tensegrity airfoil on its aerodynamic performance, we conduct a sensitivity study. To simplify the fluid-structure interaction in this aerodynamic analysis, we make several assumptions. We assume ideal flow conditions, where the fluid is incompressible, irrotational, steady, and inviscid. These idealized conditions allow us to focus on the fundamental behavior of the airfoil without the complexities introduced by viscosity and turbulence. Moreover, this assumption is common for low-speed aircraft.

The overall structure is assumed to be immersed in an infinite fluid domain, ensuring that the boundaries do not influence the flow characteristics around the airfoil. The aerodynamic forces acting on the airfoil are computed using

the panel method developed in [36], based on the approach by Hess and Smith [37] and later adopted by Boeing in the 1960s. The flow conditions are set with a Mach number of 0.1 and a Reynolds number of 2.3090×10^6.

The results of the fluid study are shown in Fig. 3. As illustrated in Fig. 3(a), the number of nodes in the structure decreases significantly as δ increases. However, as shown in Fig. 3(b), the airfoil's lift-to-drag ratio remains largely unchanged for δ values of 10^{-5}, 10^{-4}, and 10^{-3} m.

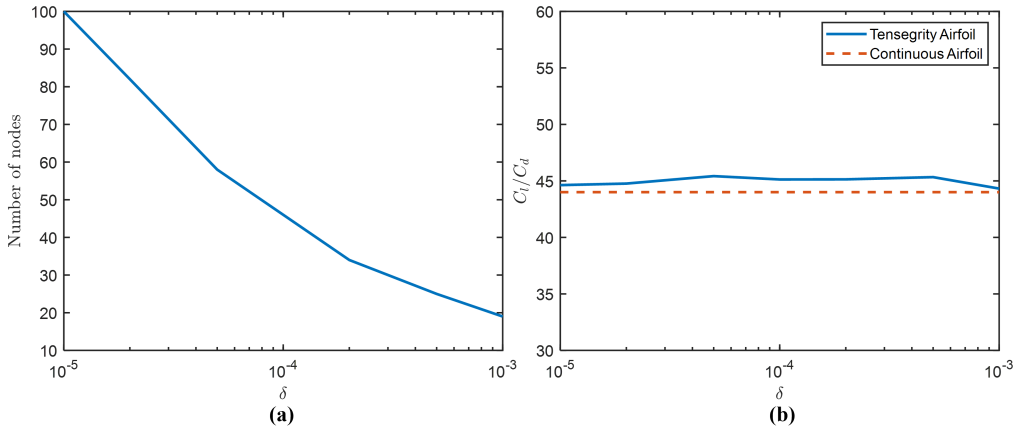

Fig. 3 Influence of error bound on node count and lift/drag coefficients. (a) The error bound δ vs. the number of nodes in the tensegrity airfoil. (b) The error bound δ vs. the lift and drag coefficient ratio C_l/C_d, the ratio for the continuous airfoil is 44.0037.

III. Experiments of Tensegrity Morphing Airfoil

Given that the precision of 3D printing and laser cutting typically does not exceed 0.1 mm, we selected an error bound of $\delta = 0.0001$ m = 0.1 m to validate our experimental NACA 2412 airfoil design. The topology generated in the second image of Fig. 2 is used to create the geometric model shown in Fig. 4. The PCB design is shown in Fig. 5. The hardware feedback loop operates as follows: the controller runs on a 3.3 V power supply and sends PWM signals to the motor driver. The motor driver, powered by 12 V, controls the two GA12-N20 motors. Motor speed is measured by a Hall sensor, which sends feedback to the controller. The Hall sensor is located on a separate encoder board, while the motor driver, the ESP32-S2 controller, and the 3.3 V/12 V power supply ports are all located on the main board.

The airfoil is printed from PLA material, with a 0.18 mm outer-diameter fishing line as the string, capable of supporting up to 15 pounds. The CAD model of the airfoil is depicted in Fig. 4. For a wing structure, one can connect the ribs with a wooden square beam, illustrated in Fig. 6, and the corresponding wing design is shown in Fig. 7. The wing maintains a uniform width across the span and incorporates five ribs, each capable of independent control. Each rib has a 400 mm chord length, and the ribs are spaced 200 mm apart along the wing span.

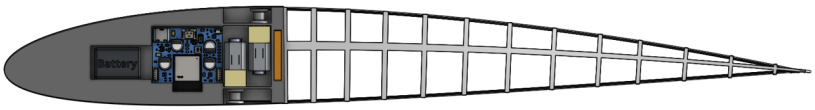

Fig. 4 The CAD model is a tensegrity airfoil with a thickness δ of 0.0001 m and a D-section spanning from 0 to 0.35 meters. The D-section houses the battery, controller (PCB board), two motors, and pulleys. The flexible tail section is printed using PLA, with the top and bottom nodes connected by fishing lines.

For the simulation, we use a quasi-static model to predict the deformation of the tensegrity airfoil [38]. The structure is assumed homogeneous and linearly elastic. For a given target cable length L_{target}, we obtain the equilibrium configuration by adjusting cable lengths and minimizing the total bending energy of the ribs, as shown in Fig 9. Specifically, the airfoil skeleton is modeled as a series of segments between adjacent ribs, each storing bending energy.

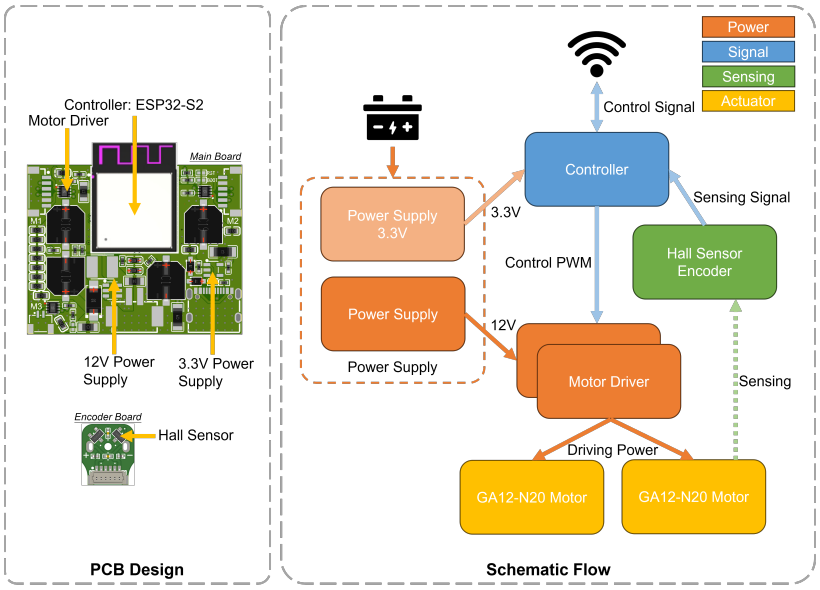

Fig. 5 The PCB design and control flow: The left box outlines key components of the custom PCB, while the right box depicts the system's control flow.

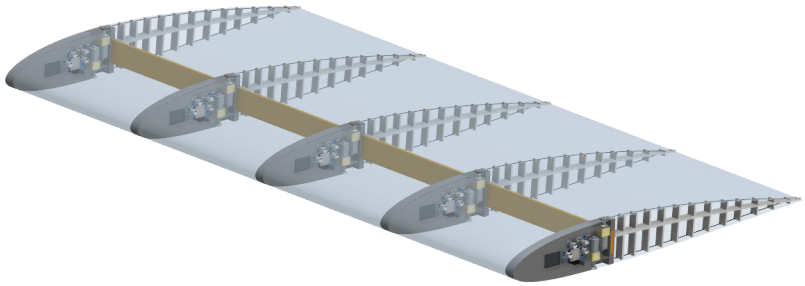

Fig. 6 The CAD model features a tensegrity morphing wing composed of five NACA2412 airfoil ribs. Each rib has a chord length of 435 mm, with a spacing of 200 mm between ribs along the wing span.

At equilibrium, the configuration solves:

$$\min_{\{\alpha_i\}} \sum_i \alpha_i^2 \quad \text{s.t.} \quad \sum_i L_i = \sum_i L(\alpha_i) = L_{\text{target}}, \tag{2}$$

where α_i is the bending angle between ribs and $L(\alpha_i)$ is the corresponding cable length. This constrained problem is solved numerically using a trust-region optimizer, with the nonlinear relation between L_i and α_i handled by iterative numerical methods (e.g., Newton–Raphson).

We compare the deformation of a single module across multiple configurations in both simulation and the physical experiment. In the simulation, the chord length is set to 0.435 m, which is the same as that of the real robot. In the experiments, we commanded the motor to encoder values of $0, -400, -500, -600, -700$, and -800, each applied with a tolerance of ± 30 to account for practical variability in hardware actuation (Fig. 10). The resulting vertical displacements were y_0, y_1, y_2, y_3, y_4, and y_5, corresponding to measured values of $0, 40, 50, 55, 63$, and 68 mm. Using the winch diameter of 6 mm and a gear ratio of 1:150, we converted each encoder command into the corresponding string-length change and applied these inputs in simulation, as shown in Fig. 8. Overall, the results (between Figs. 8 and 10) demonstrate strong agreement between the quasi-static simulation model and the real-world deformation behavior.

The bending experimental design included two tests: (1) bending the tail to achieve a consistent deflection and (2) bending the tail with linearly increasing deflections. These experiments are shown in Fig. 11. The initial configuration is presented in Fig. 11a, while Fig. 11b illustrates the consistent deflection test, and Fig. 11c illustrates the linearly

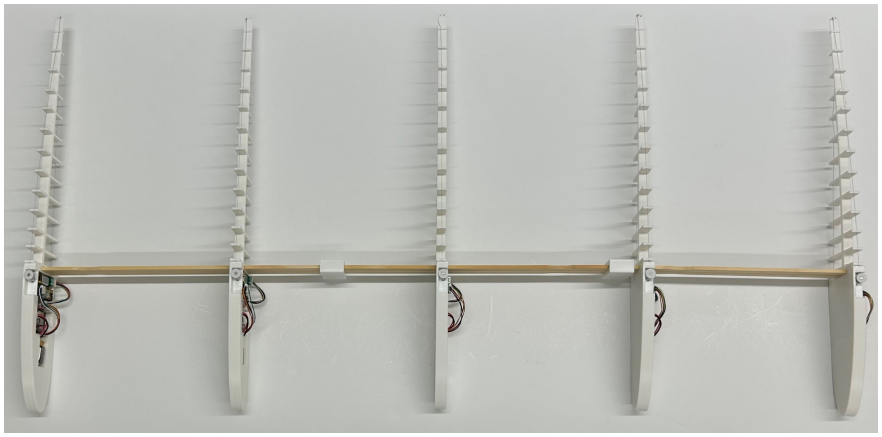

Fig. 7 The experiment rib-connected wing model.

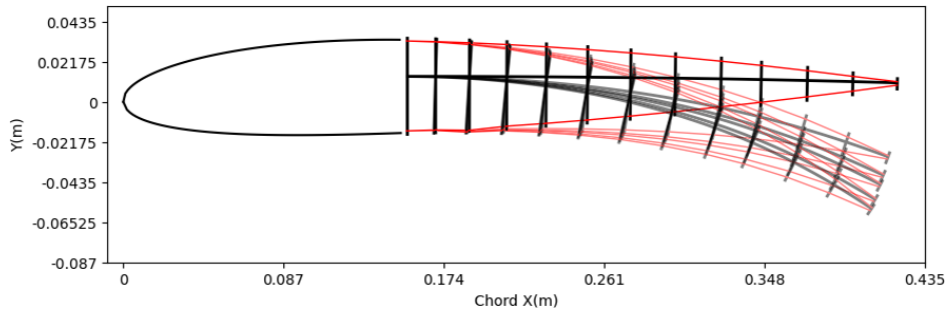

Fig. 8 Single module deforming into different configurations in the simplified simulation.

increasing deflection test.

IV. Conclusion

This paper presented the design, modeling, and experimental validation of a lightweight robotic tensegrity morphing airfoil. By discretizing a continuous airfoil using the error-bound method, we generated tensegrity-based structures with δ values ranging from 10^{-5} to 10^{-3} m and demonstrated that the lift-to-drag ratio remained effectively unchanged despite a reduction of more than 50% in node count. These results confirm that axial-load-bearing tensegrity elements can provide smooth, controllable morphing without significantly compromising aerodynamic performance.

A quasi-static model was developed to predict deformation under cable actuation, and its predictions showed strong agreement with experiments. The integrated prototype—featuring onboard electronics, a custom PCB, and compact actuation—enabled reliable shape adaptation in both single-module and multi-module tests. The full wing, consisting of a 35% chord length D-section and a PLA tensegrity tail, successfully demonstrated uniform and gradient bending across a five-rib, 435 mm-chord, 800 mm-span wing structure.

The results validate the feasibility of tensegrity architectures for morphing aerodynamic surfaces, offering a lightweight, mechanically efficient, and scalable approach to adaptive wings and bio-inspired robotic systems. Future work will incorporate skin design, closed-loop control, and wind tunnel testing to further advance tensegrity-based morphing aircraft.

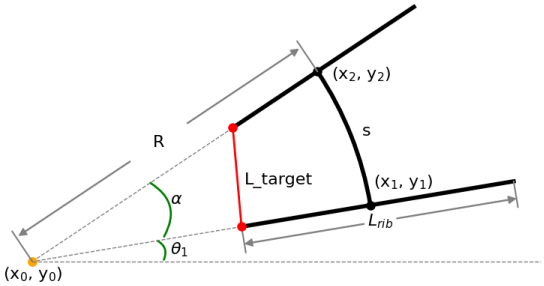

Fig. 9 Geometry of a skeleton segment and its deformation. The thick black lines represent the upper and lower ribs. The thick black curve illustrates the spine segment connecting the two ribs, with arc length s and radius of curvature R, where the connection points on the two ribs are (x_1, y_1) and (x_2, y_2). The thin red line represents the string of length L linking two threading points. The angle θ_1 defines the orientation of the bottom rib relative to the horizontal, while α characterizes the relative rotation between the two ribs. The point (x_0, y_0) denotes the center of curvature associated with the bending motion.

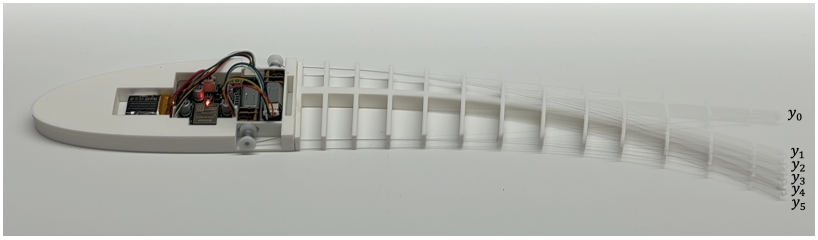

Fig. 10 Single module deforming into different configurations. The corresponding encoder controls are 0, -400, -500, -600, -700, and -800, each with a ±30 tolerance.

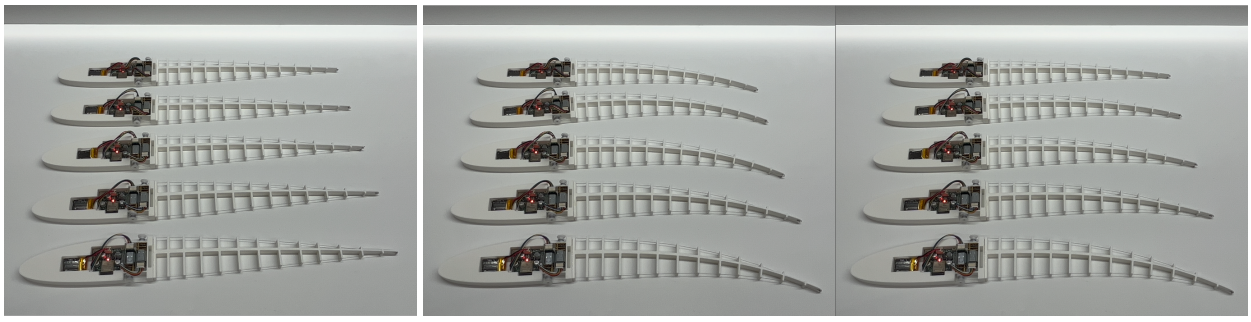

(a) **(b)** **(c)**

Fig. 11 Morphing states of the airfoils: (a) Initial state, (b) Uniform deformation of five modules, and (c) Gradual deformation of the five modules.

References

[1] Skelton, R. E., and de Oliveira, M. C., *Tensegrity Systems*, Springer US, 2009. https://doi.org/10.1007/978-0-387-74242-7.

[2] Chen, B., He, Z., Ye, F., Yang, Y., Chen, W., Ding, F., Gao, D., Zhao, Y., Lu, Z., and Jia, C., "Untethered Miniature Tensegrity Robot with Tunable Stiffness for High-Speed and Adaptive Locomotion," *Soft Robotics*, Vol. 12, No. 5, 2025, pp. 676–686. https://doi.org/10.1089/soro.2024.0178.

[3] Zhang, Y., Zheng, K., Zhao, Y., Zheng, Z., Chen, B., and Chen, M., "Collision resistant study of spherical tensegrity structures for protective drone shells," *Extreme Mechanics Letters*, Vol. 76, 2025, p. 102312. https://doi.org/10.1016/j.eml.2025.102312.

[4] Fraddosio, A., Pavone, G., and Piccioni, M. D., "Minimal mass and self-stress analysis for innovative V-Expander tensegrity cells," *Composite Structures*, Vol. 209, 2019, pp. 754–774. https://doi.org/10.1016/j.compstruct.2018.10.108.

[5] Guest, S. D., "The stiffness of tensegrity structures," *IMA Journal of Applied Mathematics*, Vol. 76, No. 1, 2011, pp. 57–66. https://doi.org/10.1093/imamat/hxq065.

[6] Xu, Y., and Chen, M., "The minimal mass tensegrity solutions to compressive and tensile loads," *International Journal of Mechanical Sciences*, Vol. 286, 2025, p. 109894. https://doi.org/10.1016/j.ijmecsci.2024.109894.

[7] Chen, B., Zhang, J., Meng, Q., Lu, Z., Zhao, C., and Jiang, H., "A dynamic model of tensegrity robotic fish considering soft fish skin and tail," *Nonlinear Dynamics*, Vol. 113, No. 1, 2025, pp. 329–353. https://doi.org/10.1007/s11071-024-10136-6.

[8] Shen, Y., Chen, M., and Skelton, R. E., "Finite word-length optimal simulation for high-dimensional dynamical systems: Examples of tensegrity structures," *Mechanical Systems and Signal Processing*, Vol. 215, 2024, p. 111415. https://doi.org/10.1016/j.ymssp.2024.111415.

[9] Amendola, A., Krushynska, A., De Piano, M., Daraio, C., Pugno, N. M., and Fraternali, F., "Mechanical modeling of the bandgap response of tensegrity metamaterials," *AIP Conference Proceedings*, Vol. 2116, AIP Publishing, 2019, p. 5. https://doi.org/10.1063/1.5114261.

[10] Mao, Z., Kobayashi, R., Nabae, H., and Suzumori, K., "Large Language Model-empowered multimodal strain sensory system for shape recognition, monitoring, and human interaction of tensegrity," , 2024. URL https://arxiv.org/abs/2406.10264.

[11] Mao, Z., Kobayashi, R., Nabae, H., and Suzumori, K., "Multimodal Strain Sensing System for Shape Recognition of Tensegrity Structures by Combining Traditional Regression and Deep Learning Approaches," *IEEE Robotics and Automation Letters*, Vol. 9, No. 11, 2024, pp. 10050–10056. https://doi.org/10.1109/LRA.2024.3469811.

[12] Sabelhaus, A. P., Zhao, H., Zhu, E. L., Agogino, A. K., and Agogino, A. M., "Model-predictive control with inverse statics optimization for tensegrity spine robots," *IEEE Transactions on Control Systems Technology*, Vol. 29, No. 1, 2020, pp. 263–277. https://doi.org/10.1109/TCST.2020.2975138.

[13] Zappetti, D., Sun, Y., Gevers, M., Mintchev, S., and Floreano, D., "Dual stiffness tensegrity platform for resilient robotics," *Advanced Intelligent Systems*, Vol. 4, No. 7, 2022, p. 2200025. https://doi.org/10.1002/aisy.202200025.

[14] Chen, M., Fraddosio, A., Micheletti, A., Pavone, G., Piccioni, M. D., and Skelton, R. E., "Analysis of clustered cable-actuation strategies of V-Expander tensegrity structures," *Engineering Structures*, Vol. 296, 2023, p. 116868. https://doi.org/10.1016/j.engstruct.2023.116868.

[15] Woods, C., and Vikas, V., "Design and Modeling Framework for DexTeR: Dexterous Continuum Tensegrity Manipulator," *Journal of Mechanisms and Robotics*, Vol. 15, No. 3, 2023, p. 031006. https://doi.org/10.1115/1.4056959.

[16] Yang, Y., Fan, L., Weng, T., Zhao, Y., Chen, B., and Li, W., "Bistable Soft Gripper With Tension Net Applied to UAV," *IEEE Robotics and Automation Letters*, Vol. 10, No. 2, 2025, pp. 1920–1927. https://doi.org/10.1109/LRA.2025.3526570.

[17] Zhao, L., Jiang, Y., She, C.-Y., Jeong, M., Dong, H., Li, A. Q., Chen, M., and Balkcom, D., "An Untethered Bioinspired Robotic Tensegrity Dolphin with Multi-Flexibility Design for Aquatic Locomotion," *2025 IEEE 8th International Conference on Soft Robotics (RoboSoft)*, 2025, pp. 1–7. https://doi.org/10.1109/RoboSoft63089.2025.11020959.

[18] Ding, F., Chen, W., Zhang, J., and Chen, B., "A high-frequency oscillating tensegrity robotic fish with wide-ranging online body stiffness adjustability," *Ocean Engineering*, Vol. 328, 2025, p. 121063. https://doi.org/10.1016/j.oceaneng.2025.121063.

[19] Zhao, L., Jiang, Y., She, C.-Y., Alberto, Q. L., Muhao, C., and Balkcom, D., "SoftRafts: Floating and Adaptive Soft Modular Robots," , December 2024. https://doi.org/10.13140/RG.2.2.25781.18400.

[20] Kobayashi, R., Nabae, H., Endo, G., and Suzumori, K., "Soft tensegrity robot driven by thin artificial muscles for the exploration of unknown spatial configurations," *IEEE Robotics and Automation Letters*, Vol. 7, No. 2, 2022, pp. 5349–5356. https://doi.org/10.1109/LRA.2022.3153700.

[21] Zhao, L., Wu, Y., Yan, W., Zhan, W., Huang, X., Booth, J., Mehta, A., Bekris, K., Kramer-Bottiglio, R., and Balkcom, D., "StarBlocks: Soft Actuated Self-connecting Blocks for Building Deformable Lattice Structures," *IEEE Robotics and Automation Letters*, 2023. https://doi.org/10.1109/LRA.2023.3284361.

[22] Zhao, L., Wu, Y., Blanchet, J., Perroni-Scharf, M., Huang, X., Booth, J., Kramer-Bottiglio, R., and Balkcom, D., "Soft Lattice Modules That Behave Independently and Collectively," *IEEE Robotics and Automation Letters*, Vol. 7, No. 3, 2022, pp. 5942–5949. https://doi.org/10.1109/LRA.2022.3160611.

[23] Zhao, L., Jiang, Y., Chen, M., Bekris, K., and Balkcom, D., "Modular shape-changing tensegrity-blocks enable self-assembling robotic structures," *Nature Communications*, Vol. 16, No. 1, 2025, p. 5888. https://doi.org/10.1038/s41467-025-60982-0.

[24] Dong, Y., Yuan, X., Ma, S., Li, S., Samy, A., and Dong, S., "Research on a novel tensegrity torus with superior shape adaptability," *Structures*, Vol. 63, 2024, p. 106283. https://doi.org/10.1016/j.istruc.2024.106283.

[25] Lee, H., Jang, Y., Choe, J. K., Lee, S., Song, H., Lee, J. P., Lone, N., and Kim, J., "3D-printed programmable tensegrity for soft robotics," *Science Robotics*, Vol. 5, No. 45, 2020, p. eaay9024. https://doi.org/10.1126/scirobotics.aay9024.

[26] Agogino, A. K., SunSpiral, V., and Atkinson, D., "Super Ball Bot-structures for planetary landing and exploration," Tech. rep., NASA, 2018. URL https://www.nasa.gov/general/super-ball-bot-structures-for-planetary-landing-and-exploration/.

[27] Islam, M. A., Rahman, A., Saha, A., and Jo, B. W., "Design, Implementation, and Test Flight of a Lightweight Camber Morphing Wing Aircraft," *AIAA AVIATION FORUM AND ASCEND 2025*, 2025, p. 3524. https://doi.org/10.2514/6.2025-3524.

[28] Menshchikov, A., and Somov, A., "Morphing wing with compliant aileron and slat for unmanned aerial vehicles," *Physics of Fluids*, Vol. 31, No. 3, 2019. https://doi.org/10.1063/1.5086976.

[29] Jia, X., Chang, T., Zhou, S., Zhang, X., Wang, S., and Zhang, Z., "Progress in Bionic Deformable Wing of Aircraft Driven by Shape Memory Alloy," *Journal of Bionic Engineering*, Vol. 22, No. 5, 2025, pp. 2236–2260. https://doi.org/10.1007/s42235-025-00744-2.

[30] Hu, K., Ge, H., Li, H., Yan, T., Zheng, X., and Wang, B., "High actuation capability and smooth-deformation piezo morphing wing based on multi-layer parallel pre-compressed MFC bimorph," *Aerospace Science and Technology*, Vol. 132, 2023, p. 108083. https://doi.org/10.1016/j.ast.2022.108083.

[31] Chen, M., Liu, J., and Skelton, R. E., "Design and control of tensegrity morphing airfoils," *Mechanics Research Communications*, Vol. 103, 2020, p. 103480. https://doi.org/10.1016/j.mechrescom.2020.103480.

[32] Shintake, J., Zappetti, D., Peter, T., Ikemoto, Y., and Floreano, D., "Bio-inspired Tensegrity Fish Robot," *2020 IEEE International Conference on Robotics and Automation (ICRA)*, IEEE, 2020, pp. 2887–2892. https://doi.org/10.1109/ICRA40945.2020.9196675.

[33] Mills, A. S., Myszka, D. H., Woods, D. C., Joo, J. J., and Murray, A. P., "The structural suitability of tensegrity aircraft wings," *AIAA Scitech 2020 Forum*, 2020, p. 0480. https://doi.org/10.2514/6.2020-0480.

[34] Zhou, H., Plummer, A. R., and Cleaver, D., "Distributed actuation and control of a tensegrity-based morphing wing," *IEEE/ASME Transactions on Mechatronics*, Vol. 27, No. 1, 2021, pp. 34–45. https://doi.org/10.1109/TMECH.2021.3058074.

[35] Liu, H., Song, J., and Luo, A., "Analysis of a tensegrity camber morphing airfoil," *Mechanics Research Communications*, Vol. 137, 2024, p. 104272. https://doi.org/10.1016/j.mechrescom.2024.104272.

[36] Drela, M., "XFOIL: An analysis and design system for low Reynolds number airfoils," *Low Reynolds Number Aerodynamics: Proceedings of the Conference Notre Dame, Indiana, USA, 5–7 June 1989*, Springer, 1989, pp. 1–12. https://doi.org/10.1007/978-3-642-84010-4_1.

[37] Hess, J. L., and Smith, A. O., "Calculation of potential flow about arbitrary bodies," *Progress in Aerospace Sciences*, Vol. 8, 1967, pp. 1–138. https://doi.org/10.1016/0376-0421(67)90003-6.

[38] Zhao, L., Jiang, Y., She, C.-Y., Chen, M., and Balkcom, D., "SoftSnap: Rapid prototyping of untethered soft robots using snap-together modules," *Soft Robotics*, 2025. https://doi.org/10.48550/arXiv.2410.19169.